RSC Advances

PAPER

View Article Online
View Journal | View Issue

Cite this: *RSC Adv.*, 2024, **14**, 29992

On the temperature dependent photoluminescence of nanoscale $LuPO_4:Eu^{3+}$ and their application for bioimaging

Jan Kappelhoff, *[a] Burkhard Greve [b] and Thomas Jüstel [a]

Received 16th February 2024
Accepted 21st July 2024

DOI: 10.1039/d4ra01190b

rsc.li/rsc-advances

This work concerns a synthesis method for efficiently luminescent $LuPO_4:Eu^{3+}$ nanoscale particles (~100 nm) as well as their temperature (77–500 K) and time dependent photoluminescence. In addition, the incubation of these particles into cells of a human lung adenocarcinomic cell line A549 is briefly presented. This points to the application for bioimaging and detection of cancer cells in the field of medical diagnostics. The emission spectra of Eu^{3+} doped $LuPO_4$ nanoparticles show four $[Xe]4f^6 \rightarrow [Xe]4f^6$ transition multiplets between 580 and 720 nm, which are typically for Eu^{3+} comprising luminescent materials, however the most intense one is the $^5D_0 \rightarrow {}^7F_4$ (696.40 nm, 1.78 eV) transition due to the crystallographic position point symmetry D_{2d} of Eu^{3+} in xenotime $LuPO_4$. Such an Eu^{3+} spectrum is rather useful for diagnostics due to the high penetration depth of 700 nm radiation into tissue.

Introduction

Rare earth doped orthophosphate nanoparticles are of increasing interest and application in biomedicine.[1–3] For example, in cancer treatment,[4] theranostics,[5] and bioimaging[6] different nanomaterials like lanthanide doped $LuPO_4$ or HfO_2 are used. They provide high chemical stability, resistance to radiation damage and a low solubility in water. This makes $LuPO_4$, whose high density (6.53 g cm^{-3}) and effective nuclear charge Z_{eff} (63.7 (ref. 7)) to an potentially attractive powder material for scintillation applications. In addition, scintillator materials require a high scintillation efficiency which correlates with a high light yield. For cancer therapy should be in the UV spectral range (<280 nm), here the tumour cells absorbing very efficiently. Unfortunately, orthophosphates, like $LuPO_4$ do not melt congruently, the single crystal cannot be procedures with the Czochralski technique.[8] Since the technology of producing high-quality $LuPO_4$ crystals has not been evolved, their polycrystalline powder materials seems to be the sole prospective alternative for their applications in bioimaging.

An improvement in detection of ionizing particles requires a constant development of scintillator materials – their performance and optical quality. It was demonstrated that for phosphors emitting in the red spectral range the imaging resolution properties are optimal.[9] Nevertheless, the scintillation and luminescence efficiency in the nanometer scale gets reduced, but lutetium based scintillator materials were reported as efficient scintillators.[10]

In the present work, nanoscale $LuPO_4$ particles with a concentration range of Eu^{3+} (0.1–40 mol%) are presented, while the temperature and time dependent photoluminescence is discussed as well. Furthermore, these particles were incubated for the first time in A549 lung cancer cells and made them visible with excitation by an UV-A emitting LED ($\lambda_{exc.} = 365$ nm).

Experimental section

Particle synthesis

The nanoscale $LuPO_4$ particles with a fixed Eu^{3+} concentration (0.1–40 mol%) were prepared by a modified sedimentation nucleation method.

First of all, $LuCl_3 \cdot 7\ H_2O$ (>99.99%, Jiayuan Advanced Materials Co., Ltd) and $Eu(CH_3COO)_3 \cdot 4\ H_2O$ (99+%, Nanosolutions GmbH) were dissolved in a stoichiometric ratio in 81 ml dest. H_2O. Further, 60 mmol $NH_4H_2PO_4$ (Merck KGaA, min. 99.99%) were dissolved in 300 ml dest. H_2O and with NaOH solution (1 mol l^{-1}) the pH value was adjusted to 12 (pH meter). Then the solution was added dropwise to the mixture with dissolved $LuCl_3 \cdot 7\ H_2O$ and $Eu(CH_3COO)_3 \cdot 4\ H_2O$ under continuous stirring for 3.5 h. As a result, a white fine-dispersed precipitate was obtained. The precipitate was separated by centrifugation, washed by using distilled water several times until a pH 7 was attained, and finally dried by washing with ethanol. The obtained $LuPO_4:Eu^{3+}$ nanoparticles were dried under vacuum to constant weight. For appropriate crystallisation, the precipiced particles were annealed for 2 h at 1000 °C.

[a]*Department of Chemical Engineering, Münster University of Applied Sciences, Stegerwaldstraße 39, D-48565 Steinfurt, Germany. E-mail: jan-kappelhoff@fh-muenster.de; tj@fh-muenster.de*

[b]*Department of Radiotherapy – Radiooncology, University Hospital Münster, Albert-Schweitzer-Campus 1, D-48149 Münster, Germany. E-mail: burkhard.greve@ukmuenster.de*

For the removal of secondary phases, the precipitate was washed under continuous stirring for 5 h at 60 °C in HNO_3/H_2O (1 : 7), followed by washing to a neutral pH value and dried at 60 °C under vacuum. The last step is the separation of the nanoparticles by means of centrifugation.

X-ray diffraction patterns

The phase formation and phase purity of the prepared nanoparticles were investigated by powder X-ray diffraction (PXRD). Accordingly, a Rigaku MiniFlex II diffractometer was used. The samples were measured in Bragg–Brentano geometry upon using x-rays at 0.15406 nm (Cu $K_{\alpha 1}$ radiation). The diffractograms were recorded between $2\theta = 10$–$80°$ with a step width of 0.02° and a speed of 5° min^{-1}.

Diffuse reflectance spectroscopy

The diffuse reflectance spectra were recorded upon employing an Edinburgh Instruments FLS920 spectrometer equipped with a custom build spectralon coated integrating sphere, a xenon arc lamp (450 W) and a cooled (−20 °C) single-photon counting photomultiplier (Hamamatsu R928). A $BaSO_4$ sample (99.99%, Sigma Aldrich) was used as a white reflectance standard (100%). The device is operated with two TMS300 monochromators (Czerny-Turner Optics) equipped with 1800 grooves per millimeter (Gr/mm).

Transmission electron microscopy (TEM)

TEM images of the nanoparticles were performed on a JEOL JEM-2100Plus transmission electron microscope. The images were detected with a resolution of 0.14 nm applying an acceleration voltage of 200 kV and different magnifications (10–100 nm).

Temperature and time resolved spectroscopy

Temperature dependent luminescence spectra were recorded on a Edinburgh Instruments FLS920 spectrometer with a liquid nitrogen cryostat from Oxford Instruments for cooling the samples to 77 K (±3 K). Temperature stabilization time was 30 s and the samples were measured between 77 and 500 K in 25 K steps.

Temperature dependent decay measurements were done on the same spectrometer and in the same time temperatures ranges and steps. The samples were excited at 390.05 nm with a pulsed Xe-arc lamp (μF920H) (450 W) flash lamp. Decay curves were recorded at 697.10 nm and was observed for 20 ms (Eu^{3+}) with 2000 channels. With an initial intensity of 4000 counts, the decay measurement was started and for detection a single photon detector (R2658P) from Hamamatsu was used.

Nanoparticle uptake and light microscopy

About 1×10^6 cells of the human lung adenocarcinomic cell line A549 (LGC-Petrochem/ATCC, Wesel, Germany) cultured in Petri dishes containing 4 ml DMEN (Sigma, Merck-Millipore, Darmstadt, Germany) based culture medium were treated either with 0.5 mg ml^{-1} $LuPO_4$:Eu^{3+} (5 mol%) nanoparticles or with 0.5 mg ml^{-1} $LuPO_4$ control nanoparticles without europium. Cells were incubated for 24 h in an incubator under humidified atmosphere of 5% CO_2 at 37 °C. Afterwards cells were washed three times with 2 ml PBS containing 0.5% (w/v) bovin serum albumin (BSA) to remove free nanoparticles.

Microscopic analysis was performed using an inverse microscope (Inverso, Cytecs, Münster, Germany). A 365 nm UV-LED was used for excitation and emission was measured at 610 nm with an exposure time of 500 ms.

Results and discussion

Phase purity of nanoscale particles

From all samples, which are comprising nanoscale $LuPO_4$ particles with a varying Eu^{3+} concentration (0.1–40 mol%) powder X-ray diffraction patterns have been recorded. These patterns are plotted in Fig. 1. To proof the presence of single phase materials, the recorded X-ray diffraction patterns (black) were compared to a reference pattern (red) of undoped $LuPO_4$ from the Pearson's Crystal Database (PCD).

The structure of Lutetium orthophosphate $LuPO_4$ is well investigated, while all powders are crystallized regardless of the Eu^{3+} ion concentration in a tetragonal crystal system belonging to the space group $I4_1/amd$ ($D\frac{19}{4h}$, #141). The structure thus comprise solely one metal site where at the Lu^{3+} ions are 8-fold coordinated by oxygen atoms with a D_{2d} local symmetry, which is adopted from Eu^{3+} ions. The local site symmetry D_{2d} affects the Eu^{3+} $[Xe]4f^6 \rightarrow [Xe]4f^6$ transition intensity and splitting, which finally determines the obtained Eu^{3+} emission pattern. The phosphate groups (PO_4^{3-}) form a slightly distorted tetrahedron.

Nanoparticle morphology

An embodiment of an average particle dize distribution of all prepared nanoparticle batches with a mean median diameter of around 120 nm is shown in Fig. 2. The results of these dynamic light scattering measurements (DLS) are not in agreement with crystal size calculations by using the Debye–Scherrer equation (20 nm). The images below show a typical impression of the agglomerates as obtained by transmission electron microscopy (TEM).

Concentration quenching & luminescence spectroscopy

The emission specta of as-prepared $LuPO_4$:Eu^{3+} samples as function of the activator concentration (0.1–40 mol%) are shown in Fig. 3. In order to investigate the concentration quenching, the integrated emission intensities for the transitions ($^7F_{1,2,3}$) were calculated but just the integral of the $^5D_0 \rightarrow {}^7F_4$ transitions is shown by the right graph. For the other transitions ($^7F_{1,2,3}$) similar results were observed, however, these are not depicted here. Concentration quenching for Eu^{3+} is well-known in solid state compounds, for example in Gd_2O_3 (ref. 11) and La_2O_3.[12] The optimal integral intensity is observed at an Eu^{3+} content of 15 mol% and thus the following measurements were made with this sample.

In Fig. 4 the excitation, emission, and diffuse reflectance spectra of nanoscale $LuPO_4$:Eu^{3+}(15 mol%) are presented. The

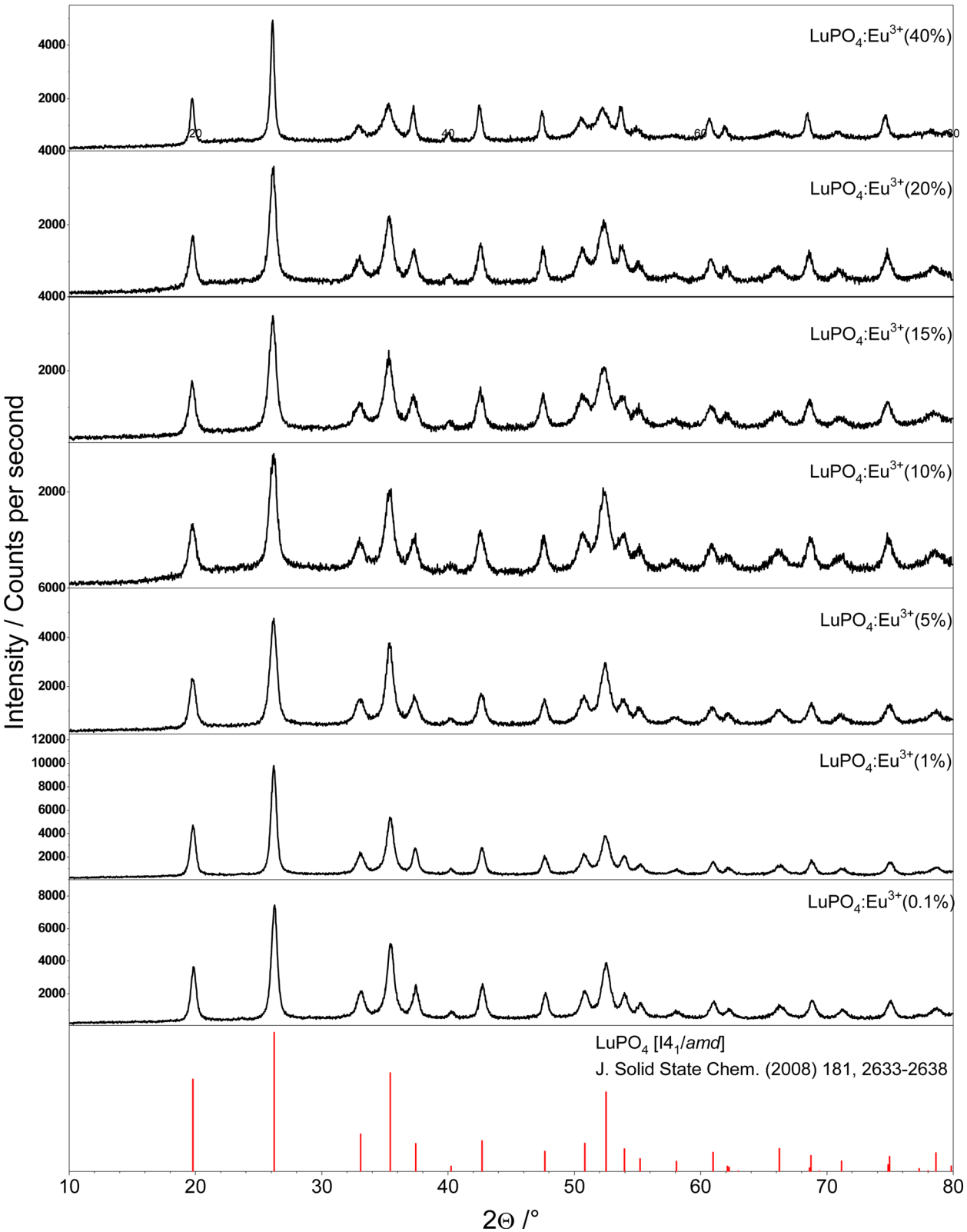

Fig. 1 Powder X-ray diffraction patterns of $LuPO_4$:Eu^{3+} (0.1–40 mol%) compared to the reference database pattern of tetragonal $LuPO_4$ (mineral type: xenotime).

blue line shows the diffuse reflectance spectrum compared to $BaSO_4$. A high reflectance over the whole recored wavelength range, *i.e.* between 250–800 nm is recognizable, which proofs a high sample quality with a low defect density resulting in a pure white body colour. In addition, the Eu^{3+} absorption lines as mentioned below are weak but visible in the reflection spectrum.

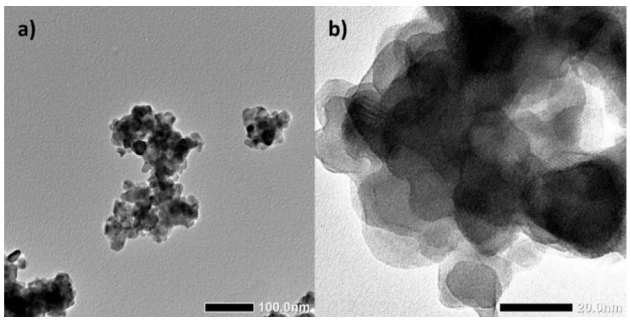

Fig. 2 TEM images of $LuPO_4$:Eu^{3+}(15 mol%) nanoparticles which forms agglomerates in a diameter of around 100 nm (a) while the crystallite size is about 20 nm (b).

An excitation spectra (black line) was monitored at the most intense emission wavelength, *viz.* at 696.40 nm and reveals well-resolved [Xe]$4f^6$ → [Xe]$4f^6$ lines, which stem from the $^7F_0$ → $^5H_3$ (319.6 nm, 3.88 eV), $^7F_0$ → $^5D_4$ (363.2 nm, 3.41 eV), $^7F_0$ → $^7L_7$ (376.6 nm, 3.29 eV), $^7F_0$ → $^7L_6$ (395.2 nm, 3.14 eV), $^7F_0$ → $^5D_3$ (418.6 nm, 2.96 eV), $^7F_0$ → $^5D_2$ (466.2 nm, 2.66 eV), and $^7F_0$ → $^5D_1$ (527.2 nm, 2.35 eV) intraconfigurational transitions. Beyond the sharp lines, a broad band originating from the O^{2-} → Eu^{3+} charge transfer (CT) between 205 and 265 nm is clearly visible. The rather high energy of the position of the CT transition is justified by the quite large interatomic distances of 2.2655 Å[13] for Eu^{3+} in the $LuPO_4$ host.

Furthermore, the emission spectra recorded for 395.20 nm excitation were recorded. The sharp [Xe]$4f^6$ → [Xe]$4f^6$ lines originate from 4f-4f transition, *viz.* $^5D_0$ → $^7F_1$ (magnetic dipole induced, 595.90 nm, 2.08 eV), $^5D_0$ → $^7F_2$ (hypersensitive electric dipole induced, 619.65 nm, 2.00 eV), $^5D_0$ → $^7F_3$ (650.80 nm, 1.91 eV), and $^5D_0$ → $^7F_4$ (696.40 nm, 1.78 eV). The latter at 696.40 nm is the most intense one and has a much higher emission integral than the $^5D_0$ → $^7F_{1,2,3}$ transition due to the local symmetry

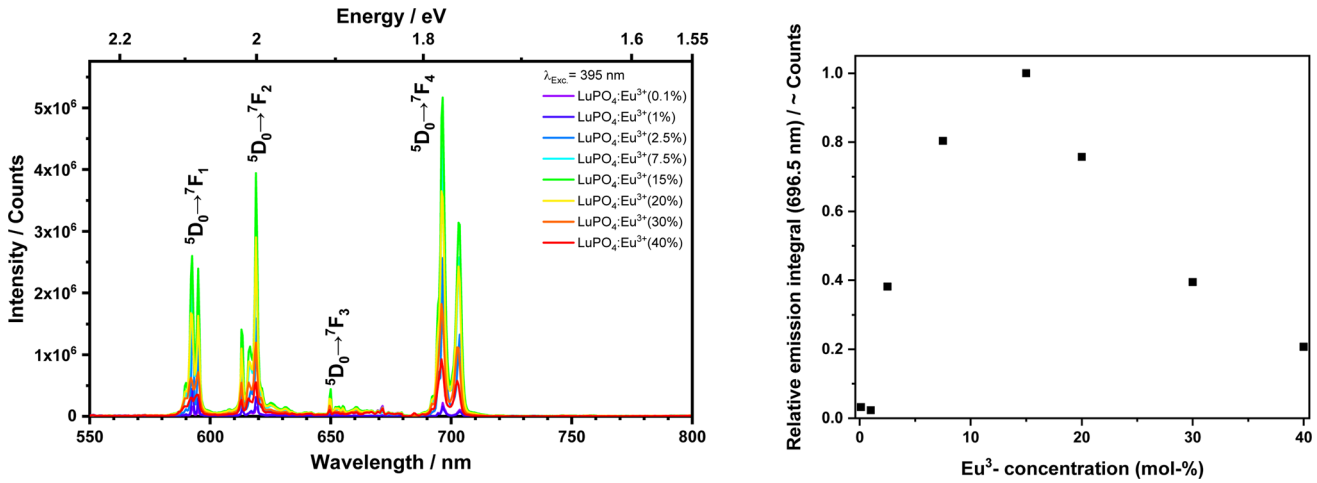

Fig. 3 Emission spectra (left) and emission integrals $^5D_0$ → $^7F_4$ (right) upon excitation at 395 nm from the $LuPO_4$:Eu^{3+}(0.1–40 mol%) sample at room temperature.

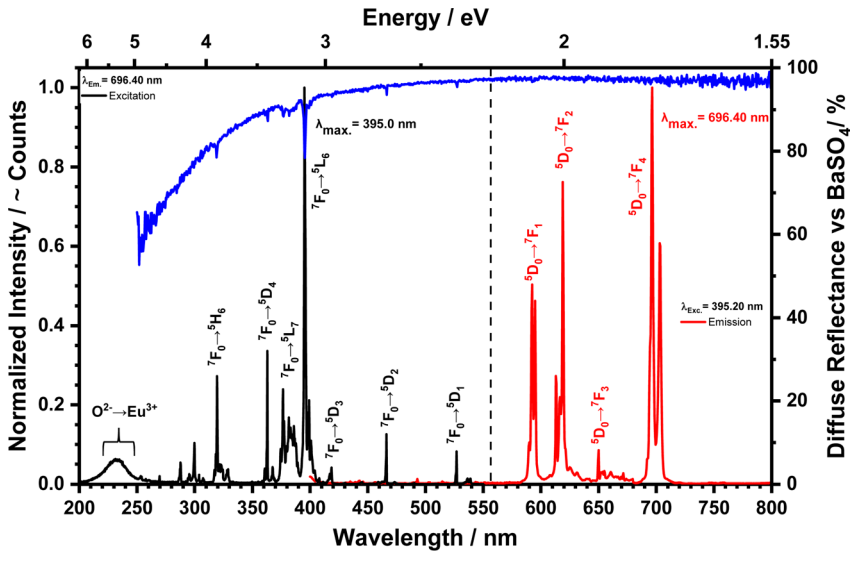

Fig. 4 Diffuse reflectance *vs.* $BaSO_4$, excitation and emission spectra of the $LuPO_4$:Eu^{3+}(15 mol%) sample at room temperature.

of Eu^{3+} in such tetragonal crystalline environment. Host lattices with a high symmetry, which are doped by Eu^{3+} exhibit an intense emission of the $^5D_0 \rightarrow {}^7F_1$ transition.[14] With decreasing symmetry, the $^5D_0 \rightarrow {}^7F_{2,3,4}$ transitions increase in intensity. Skaudzius *et al.*[15] published a study of Eu^{3+} ($^5D_0 \rightarrow {}^7F_4$ transition) luminescence in different orthophosphates and garnets as host materials. They figured out that an increasing average electronegativity, *i.e.* decrease of the basicity in octahedral and tetrahedral sites in the structure also led to an increasing intensity of the $^5D_0 \rightarrow {}^7F_4$ transition.

Temperature dependent spectroscopy

In addition, the thermal quenching behaviour of the sample with the highest emission intensity (15 mol% Eu^{3+}) was investigated. Fig. 5 shows the excitation spectra with a fixed emission wavelength at 696.40 nm between 77–500 K. The corresponding excitation transitions are listed above with the most intense $^7F_0 \rightarrow {}^5L_6$ at 395.20 nm and associated integrals as a function of the temperature are shown in Fig. 5 on the right side. A noticeable trend can be identified that the integrals of transition $^7F_0 \rightarrow {}^5L_6$ decrease with increasing temperature. Noticeable is that the excitation band shifts from the CT to higher wavelengths (228 to 237 nm). This red-shift is likely caused by thermal expansion of the Eu^{3+} surrounding, which eases the electron transfer from the ligands to the metal ion, which is then formally reduced to the larger Eu^{2+}.[16]

The left graph of Fig. 6 shows the emission spectra record upon a fixed excitation wavelength at 395.20 nm between 77 and 500 K. The corresponding excitation transitions are listed above with the most intense $^5D_0 \rightarrow {}^7F_4$ at 696.40 nm, while the associated integrals as a function of the temperature are shown in Fig. 6 on the right side. A noticeable trend can be identified that the integrals of transition $^5D_0 \rightarrow {}^7F_4$ decrease with increasing temperature.

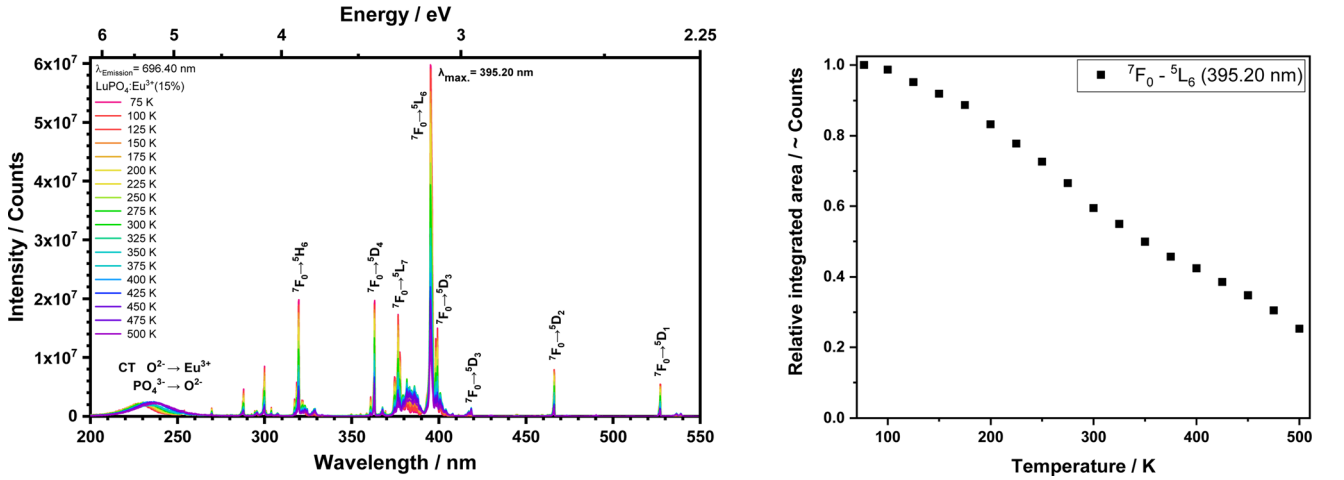

Fig. 5 Excitation spectra (left) and PL integrals (right) from the $LuPO_4:Eu^{3+}$(15 mol%) sample at a fixed emission wavelength at 696.40 nm in a temperature between 77 and 500 K.

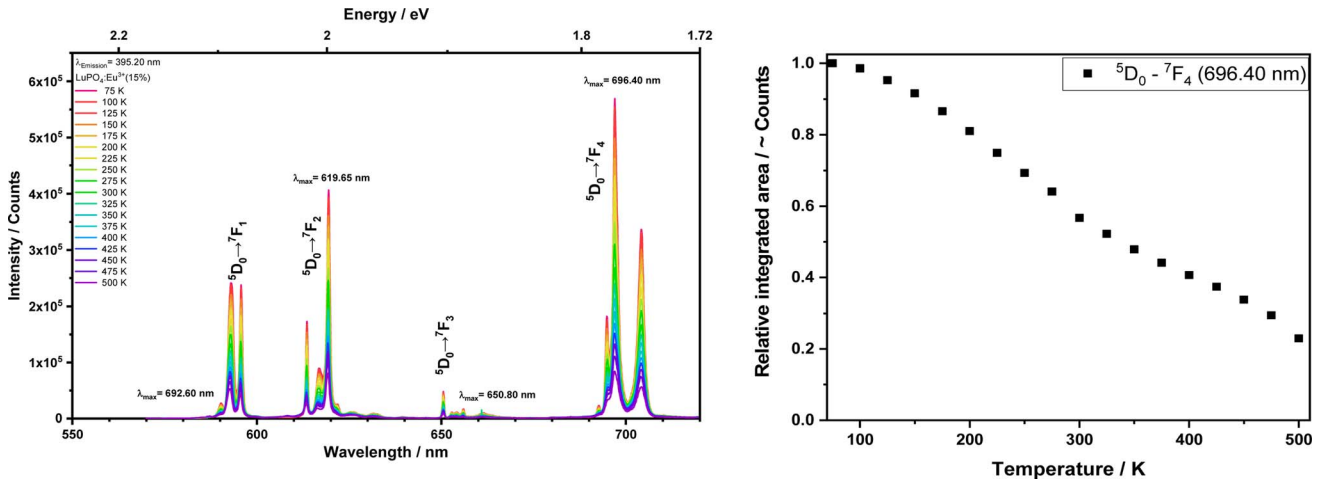

Fig. 6 Emission spectra (left) and integrals (right) from the $LuPO_4:Eu^{3+}$(15 mol%) sample upon excitation at 395.20 nm ($^5D_0 \rightarrow {}^7F_4$)in the temperature range between 77 and 500 K.

Decay curves as function of temperature

The decay curves for varying emission wavelength 696.40 nm ($^5D_0 \rightarrow {}^7F_4$) upon 395.20 nm excitation are presented in Fig. 7. They are biexponential, practically identical for all investigated transitions $^5D_0 \rightarrow {}^7F_{1,2,3}$, which confirms that Eu^{3+} occupy two crystallographic site. The decay times are about 2.8 (500 K) and 4 ms (77 K), thus in very good agreement with those reported for other Eu^{3+} phosphors.[17,18] Such long decay constants are characteristic for electric-dipole forbidden $[Xe]4f^6 \rightarrow [Xe]4f^6$ transitions.

These values for the single exponential decay curves substantiate that there is almost no luminescence quenching of Eu^{3+} in the investigated material. The drop of the emission lifetime indicates the presence of typical temperature quenching behavior between Eu^{3+} ions. In the thermal quenching process, energy transfer occurs from Eu^{3+} to other defect states/level by thermal phonon assistance.

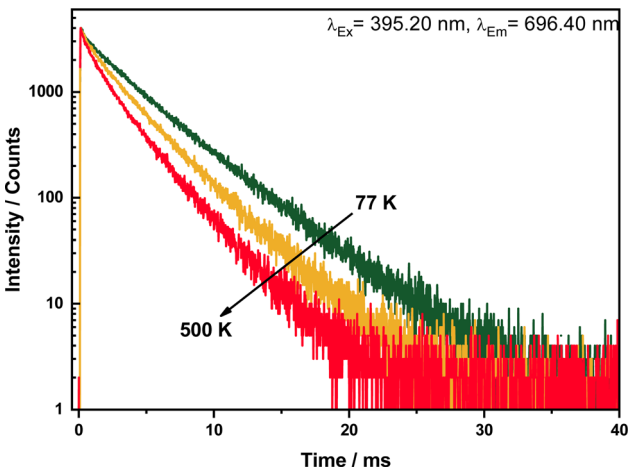

Fig. 7 Decay curves of $LuPO_4$:Eu^{3+}(15 mol%) sample upon excitation at 395.20 nm and emission at 696.40 nm in a temperature range between 77–500 K.

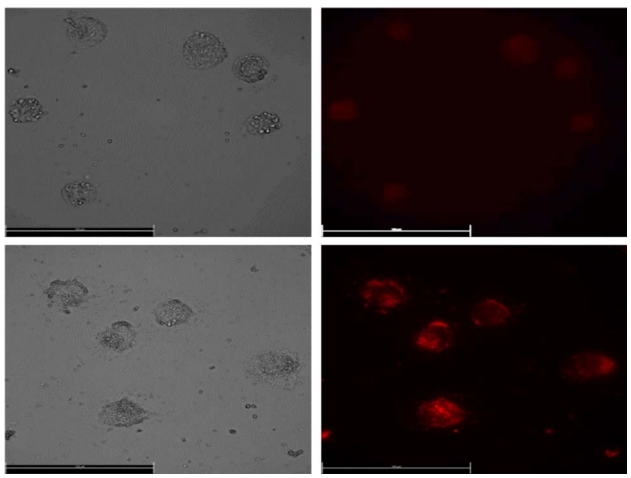

Fig. 8 Images of human lung adenocarcinomic cell line A549 incubated with $LuPO_4$:Eu^{3+}(15 mol%) nanoparticles.

Application for bioimaging

$LuPO_4$ is known as an FDA approved inorganic material and *e.g.* used as a $^{177}LuPO_4$ radiomarker (Fig. 8).[19]

For the application of these efficiently deep red emitting nanoparticles, they were incubated in A549 human lung cancer cells. Due to the excitation with a 365 nm UV-LED and the emission was measured at 610 nm *via* fluorescence microscopy. To our knowledge, that is the first time Eu^{3+} doped $LuPO_4$ nanoparticles were incubated in human lung cancer cells. The emission maximum of 696.40 nm is located in the wavelength range of 650–900 nm, where hemoglobin and water, the major absorbers of visible and infrared light, have their lowest absorption coefficient.[20] The intense red Eu^{3+} emission can be clearly visualized and turns this material to a potential alternative for the application in bioimaging/detection.

Conclusions

This works deals with a solid solution of nanoscale $LuPO_4$ in which Eu^{3+} (0–15 mol%) is incorporated. From $LuPO_4$:Eu^{3+} (15 mol%) temperature as well time dependent luminescence properties were studied in more detail. The highest emission intensity integral was detected for the sample doped by 15 mol% Eu^{3+}. Therefore, its thermal quenching curve between 77–500 K was recorded. In addition, the nanoparticles were inserted in human lung adenocarcinomic cell line A549, while it turned out that these particles are useful for optical bioimaging. In former paper it was reported that $LuPO_4$ doped with Pr^{3+} is useful as a radiosensitizer in cancer therapy. Therefore, the next goal w.r.t these nanoscale particles is its modification such a way that cancer therapy and bioimaging could be combined. Therefore, $LuPO_4$ co-doped with Pr^{3+} and Eu^{3+} will be in the focus of future work.

Data availability

The data that support the findings of this study are available from the corresponding author upon reasonable request and are available in the article.

Conflicts of interest

There are no conflicts of interest to declare.

Acknowledgements

The authors are grateful to the European Union (Europäische Union, Europäischer Fonds für regionale Entwicklung (EFRE-0600059)) for generous financial support. We thank Dr Wolfgang Göhde and Marina Lezhnina from Quantum Analysis, Münster for support in the generation of microscopic cell pictures.

References

1 G. Bao, S. Mitragotri and S. Tong, *Annu. Rev. Biomed. Eng.*, 2013, **15**, 252–282, DOI: 10.1146/annurev-bioeng-071812-152409.

2 V. K. Arivarasan, K. Loganathan and P. Janarthanan, *Nanotechnology in Medicine*, 2021, DOI: 10.1007/978-3-030-61021-0.
3 J.-C. G. Bünzli, *Chem. Rev.*, 2010, **110**(5), 2729–2755, DOI: 10.1021/cr900362e.
4 T. Tran, J. Kappelhoff, T. Jüstel, R. Anderson and M. Purschke, *Int. J. Radiat. Biol.*, 2022, **28**, 1–11, DOI: 10.1080/09553002.2022.2027541.
5 L. R. H. Gerken, K. Keevend, Y. Zhang, F. H. L. Starsich, C. Eberhardt, G. Panzarasa, M. T. Matter, A. Wichser, A. Boss, A. Neels and I. K. Herrmann, *ACS Appl. Mater. Interfaces*, 2019, **11**, 437–448, DOI: 10.1021/acsami.8b20334.
6 F. W. Pratiwi, C. W. Kuo, B. C. Chen and P. Chen, *Nanomedicine*, 2019, **14**(13), 1759–1769, DOI: 10.2217/nnm-2019-0105.
7 A. Lempicki, E. Berman, A. J. Wojtowicz, M. Balcerzyk and L. A. Boatner, *IEEE Trans. Nucl. Sci.*, 1993, **40**(4), 384–387, DOI: 10.1109/NSSMIC.1992.301128.
8 J. S. Neal, L. A. Boatner, M. Spurrier, P. Szupryczynski, and C. L. Melcher, *Hard X-Ray and Gamma-Ray Detector Physics and Penetrating Radiation Systems VIII*, 2006, vol. 6319, pp. 631901, DOI: 10.1117/12.683884.
9 P. Reineck and C. G. Brant, *Adv. Opt. Mater.*, 2017, **5**(2), 1600446, DOI: 10.1002/adom.201600446.
10 V. Vistovskyy, T. Malyi, A. Vaskiv, M. Chylii, N. Mitina, A. Zaichenko, A. Getkin and A. Voloshinovskii, *J. Lumin.*, 2016, **179**, 527–532, DOI: 10.1016/j.jlumin.2016.07.064.
11 O. Meza, E. G. Villabona-Leal, L. A. Diaz-Torres, H. Desirena, J. L. Rodriguez-Lopez and E. Perez, *J. Phys. Chem.*, 2014, **118**(8), 1390–1396, DOI: 10.1021/jp4119502.
12 V. Dordevic, Z. Antic, M. G. Nikolic and M. D. Dramicanin, *Journal of Research in Physics*, 2013, **37**(1), 47–54, DOI: 10.1038/86684.
13 F. X. Zhang, M. Lang, R. C. Ewing, J. Lian, Z. W. Wang, J. Hu and L. A. Boatner, *J. Solid State Chem.*, 2008, **118**(10), 2633–2638, DOI: 10.1016/j.jssc.2008.06.042.
14 J. Zhang, G. Cai, W. Wang, L. Ma, X. Wang and Z. Jin, *Inorg. Chem.*, 2020, **59**(4), 2241–2247, DOI: 10.1016/j.jlumin.2016.07.064.
15 R. Skaudzius, A. Katelnikovas, D. Enseling, A. Kareiva and T. Jüstel, *J. Lumin.*, 2014, **147**, 290–294, DOI: 10.1016/j.jlumin.2013.11.051.
16 D. den Engelsen, T. G. Ireland, R. Dhillon, G. Fern, P. G. Harris and J. Silver, *ECS J. Solid State Sci. Technol.*, 2016, **5**(5), R59–R66, DOI: 10.1149/2.0071605jss.
17 M. L. Debasu, D. Ananias, A. G. Macedo, J. Rocha and L. D. Carlos, *J. Phys. Chem. C*, 2011, **115**(31), 15297–15303, DOI: 10.1021/jp205093x.
18 P. J. Dereń and J. C. Krupa, *J. Lumin.*, 2003, **102**, 386–390, DOI: 10.1016/S0022-2313(02)00529-X.
19 H. Yousefnia, E. Radfar, A. R. Jalilian, A. Bahrami-Samani, S. Shirvani-Arani, A. Arbabi and M. Ghannadi-Maragheh, *J. Radioanal. Nucl. Chem.*, 2010, **287**, 199–209, DOI: 10.1007/s10967-010-0676-4.
20 R. Weissleder, *Nat. Biotechnol.*, 2001, **19**(4), 316–317, DOI: 10.1038/86684.